RSC Advances

PAPER

View Article Online
View Journal | View Issue

Open Access Article. Published on 02 March 2026. Downloaded on 3/21/2026 1:02:11 PM.
This article is licensed under a Creative Commons Attribution-NonCommercial 3.0 Unported Licence.

Check for updates

Cite this: *RSC Adv.*, 2026, **16**, 11686

Hybrid polythiophene–metal composites as promising sensing materials for chemical warfare agents and chlorofluorocarbons

Sarita Yadav, Uday Bhan Yadav and Madhulika Gupta *

The effective detection of toxic industrial chemicals and chemical warfare agents (CWAs) demands sensing materials that combine high sensitivity with low production cost. Conducting polymers such as polythiophene (PTh) offer structural flexibility, yet their intrinsic electronic properties often limit sensing performance. In this work, PTh is doped with first-row transition metals (TM = Sc–Zn), and the changes in structural stability, electronic structure, and magnetic properties are assessed using spin-polarized density functional theory (DFT). Different spin multiplicities were evaluated to identify energetically favorable configurations. Among the investigated systems, Cr@PTh (septet) and Fe@PTh (quintet) exhibit the strongest thermodynamic stability, with binding energies of −5.37 and −3.47 eV, respectively. However, the narrow energy gap in Cr limits its sensing potential, despite improved structural stability, while Fe doping provides a balanced combination of stability, electronic tunability, and reactivity, positioning Fe@PTh as the most promising candidate. Adsorption studies of Fe@PTh toward representative CWAs (HCN, NCCl, NCBr, NCCN, and AsH_3) and chlorofluorocarbons (CFC-11, CFC-12) further reveal interaction energies ranging from −2.37 to −44.79 kcal mol^{-1}. These interactions induce pronounced charge redistribution and band-gap variations of up to 0.41 eV, as supported by density-of-states and frontier-orbital analyses. Reduced density gradient (RDG) isosurface visualizations further elucidated the nature of non-covalent interactions. These results demonstrate the potential of TM@PTh composites, particularly Fe@PTh, as tunable, low-cost sensing materials capable of selectively detecting both highly reactive and environmentally persistent toxicants. This study provides a computational framework to guide the future experimental development of TM-polymer-based chemical sensors.

Received 24th January 2026
Accepted 24th February 2026

DOI: 10.1039/d6ra00636a

rsc.li/rsc-advances

1. Introduction

Organic–inorganic hybrid materials have emerged as a prominent class of functional materials owing to their ability to synergistically combine the distinct advantages of both organic and inorganic components. These integrations result in composites with superior mechanical strength, enhanced chemical stability, and tunable physicochemical properties. Consequently, these materials are being extensively examined across a wide range of applications, including catalysis, energy storage solutions, and sensing technologies.[1–5] Polymer-metal composites, consisting of transition metal (TM) nanoparticles dispersed within a polymer matrix, harness the complementary advantages of both constituents, combining the mechanical flexibility and ease of processing inherent to polymers with the electronic, magnetic, and catalytic functionalities of metals.[6–10] This synergistic interplay facilitates the design and development of multifunctional materials engineered for advanced applications in optoelectronics, chemical sensing, and electrolysis. In these domains, the high surface area and reactivity of metal nanoparticles play a crucial role in enhancing the overall performance of the material.[11–15]

Among conducting polymers, polythiophene (PTh) has garnered considerable attention due to its high electrical conductivity, excellent thermal and environmental stability, and ease of chemical modification.[16–20] PTh, composed of repeating thiophene units, is a five-membered aromatic ring containing sulfur, exhibiting a delocalized π-electron system that promotes efficient charge transport. This intrinsic electronic signature renders PTh suitable for applications in photovoltaic devices, organic electronics, and sensing platforms. The integration of inorganic nanoparticles, particularly metal-based nanostructures, into the PTh matrix enables further modulation of its electronic properties and the provision of novel functionalities through interfacial interactions. These hybrid nanocomposites thus offer significant potential for high-performance applications in biosensing, electrocatalysis, and environmental monitoring.

Numerous studies highlight the diverse application potential of metal-decorated PTh composites. For instance, Bagheri

Computational Biophysics Lab, Department of Chemistry & Chemical Biology, Indian Institute of Technology (Indian School of Mines), Dhanbad, Jharkhand, 826001, India. E-mail: madhulikagupta@iitism.ac.in

© 2026 The Author(s). Published by the Royal Society of Chemistry

Open Access Article. Published on 02 March 2026. Downloaded on 3/21/2026 1:02:11 PM.
This article is licensed under a Creative Commons Attribution-NonCommercial 3.0 Unported Licence.

et al. synthesized PTh–Ag nanocomposites for use in needle-trap devices, demonstrating their efficacy in detecting polycyclic aromatic hydrocarbons.[21] Similarly, Zhao *et al.* developed gold nanoparticle (AuNPs)-decorated PTh composites as electrochemical sensors, exhibiting high sensitivity and selectivity for detecting dopamine.[22] Umeda *et al.* employed electrochemical polymerization to synthesize PTh/Au and PTh/Pd composites, which demonstrated excellent catalytic performance in carbon–carbon coupling reactions.[23] Similarly, AuNPs-PTh composites have been employed for the selective detection of hydrazine, while PTh-Ni systems have shown enhanced electrical conductivity with increasing Ni content.[24] Additional examples include Pd/PTh composites, which are effective in Suzuki–Miyaura cross-coupling reactions,[25] and PTh-Ag nanocomposites that demonstrate catalytic activity in the reduction of 4-nitrophenol to 4-aminophenol.[26] The incorporation of AuNPs into PTh also shows enhanced electron transfer kinetics, reinforcing their potential for optical and electrochemical biosensing applications.[27] With increasing environmental and industrial demand for sustainable and economically viable alternatives, research efforts are focused on investigating the implementation of earth-abundant, first-row TMs (from Sc to Zn) as substitutes for expensive noble metals. This shift is crucial in the context of global challenges, including the detection and neutralization of chemical warfare agents (CWAs) and chlorofluorocarbons (CFCs), whose uncontrolled release poses serious environmental and toxicological hazards.

Although CWAs were originally deployed in warfare during World War 1, they have been extensively used since then in various industrial applications, including ore processing, metal degreasing, pesticide synthesis, and pharmaceutical manufacturing.[28,29] Their high toxicity, environmental persistence, and potential for aerosolized dispersion make them particularly dangerous.[30,31] CWAs are typically classified into four major categories based on their physiological effects: blister agents, nerve agents, pulmonary agents, and blood agents.[32,33] Among these, blood agents, such as hydrogen cyanide (HCN), cyanogen chloride (NCCl), and arsine (AsH_3), are extremely lethal due to their ability to disrupt cellular respiration, cause acute respiratory failure, and neurological damage.[34–37] In parallel, chlorofluorocarbons (CFCs), widely used as refrigerants, aerosol propellants, and cleaning solvents, have been identified as major contributors to climate change and ozone layer depletion.[38] Exposure to these volatile substances, including trichlorofluoromethane (CFC-11) and dichlorodifluoromethane (CFC-12), has been linked to respiratory and other health disorders due to their atmospheric longevity and bioaccumulative nature.[39,40] Several analytical approaches, including Raman spectroscopy, ion mobility spectroscopy, X-ray and thermal neutron analysis, and chromatographic techniques, have been employed for the detection of toxic gases.[41–45] However, these conventional methods typically involve expensive instrumentation, lengthy analysis time, and complex operational requirements, limiting their applicability for continuous, real-time monitoring and underscoring the need for sensitive, rapid, and cost-effective sensing materials.[46]

This underscores the need for developing low-cost, earth-abundant alternatives with customized properties and strong analyte interactions. Notably, to date, no hybrid system based on PTh embedded with TMs (PTh@TMs) has been specifically designed or reported for the detection of CFCs and CWAs. The motivation behind exploring PTh@TM systems arises from their complementary features- PTh offers high conductivity, environmental stability, and tunable electronic structure, while first-row TMs contribute variable oxidation states and unfilled d orbitals that can enhance adsorption and charge–transfer interactions with analytes. Such synergistic effects are expected to improve sensing performance towards CWAs and CFCs, while maintaining cost-effectiveness and sustainability compared to noble-based systems. In this context, the present study explores the potential of PTh-based composites functionalized with first-row TMs as sensing materials for the detection of CWAs and CFCs. The distinct electronic configurations and variable oxidation states of these TMs profoundly influence the structural and electronic properties of the PTh matrix, potentially enhancing its interaction and sensitivity towards toxic analytes. To probe these effects, TM@PTh composites have been systematically investigated here for their geometric, electronic, and adsorption characteristics using density functional theory (DFT). Spin-polarized calculations have been performed to accurately capture the influence of unpaired electrons and magnetic properties inherent to the TMs, providing a comprehensive understanding of composite behavior upon gas exposure. The analytes of interest include highly toxic CWAs, such as AsH_3, NCCl, HCN, cyanogen bromide (NCBr), and cyanogen (NCCN) as well as environmentally persistent CFC-11 and CFC-12. Key descriptors such as adsorption energy, charge transfer, frontier molecular orbital (FMO) distribution, and density of states (DOS) were computed to assess the sensing performance of each composite. This detailed investigation shows that Fe@PTh has promising potential for selective and sensitive detection of CWAs and CFCs. The insights obtained from this study inform future experimental design and pave the way for integrating TM@Ph composites into scalable, robust, cost-effective, and real-time sensor technologies for environmental monitoring and defense applications.

2. Computational details

All geometry optimizations were carried out in the gas phase without any symmetry constraints using the density functional theory (DFT) framework employing B3LYP[47–49] hybrid functional in combination with a mixed basis set, comprising the pseudopotential basis set (LANL2DZ)[50] and all-electron Pople basis set (6-311G(d,p)),[51] using the Gaussian 16 software.[52] The first-row TM atoms, *i.e.*, Sc–Zn, were described using the Los Alamos effective-core potential (LANL2DZ) basis set, while the 6-311G(d,p) was utilized for the other atoms. Grimme's dispersion correction was employed to account for long-range van der Waals interactions, which are essential for an accurate description of the system.[53,54] Frequency analysis confirmed that the optimized geometries correspond to a true minimum,

Open Access Article. Published on 02 March 2026. Downloaded on 3/21/2026 1:02:11 PM.
This article is licensed under a Creative Commons Attribution-NonCommercial 3.0 Unported Licence.

as no imaginary frequencies were perceived. All calculations were performed using unrestricted (spin-polarized) DFT to accurately describe the open-shell nature of TM systems. Broken-symmetry DFT was not required as each complex contains a single TM center and does not involve antiferromagnetically coupled spins. To ensure the reliability of the open-shell solutions, the expectation values of $\langle S^2 \rangle$ were monitored for all optimized geometries. The calculated $\langle S^2 \rangle$ were found to be close to the ideal $S(S+1)$ values for their respective multiplicities, indicating negligible spin contamination.

TM atoms were modeled in their neutral state to systematically evaluate intrinsic TM-PTh interactions without additional electrostatic contributions from counterions. This approach enables direct assessment of binding strength, electronic modulation, and magnetic effects induced by TM incorporation. Neutral-near-zero-valent metals are experimentally accessible *via* vapor deposition or reducing conditions and can be stabilized by coordination to sulfur sites after oxidation. Although cationic species may form under oxidative doping, explicit modeling of charge systems requires inclusion of counterions and solvation effects, which is beyond the scope of the current work. The binding energy (E_{bin}) of the TM@PTh complexes was obtained using the following equation:

$$E_{\text{bin}} = E_{\text{TM@PTh}} - (E_{\text{TM}} + E_{\text{PTh}}) \quad (1)$$

where $E_{\text{TM@PTh}}$, E_{TM}, and E_{PTh} represent the energies of the TM@PTh complexes, the TM atoms, and PTh, respectively.

Furthermore, the interaction energies (E_{int}) of considered CWAs (NCCl, NCBr, NCCN, HCN, and AsH_3) and CFCs (CFC-11 and CFC-12) over the active sites of TM@PTh complexes were determined using the following equation:

$$E_{\text{int}} = E_{\text{TM@PTh–CWAs/CFCs}} - (E_{\text{TM@PTh}} + E_{\text{CWAs/CFCs}}) \quad (2)$$

where $E_{\text{TM@PTh–CWAs/CFCs}}$, $E_{\text{TM@PTh}}$, and $E_{\text{CWAs/CFCs}}$ represent the energy of the considered entity interacting over the active site of TM@PTh, energy of TM@PTh complexes, and energy of respective CWAs/CFCs, respectively. To ensure the accuracy of the values of interaction energies, basis set superposition errors (BSSE) were accounted for by applying the counterpoise correction method to compute E_{BSSE}.[55] Additionally, the structural and electronic properties of TM@PTh complexes were examined to assess their sensitivity to CFCs and CWAs.

To investigate and visualize non-covalent interactions (NCIs), the reduced density gradient (RDG) approach was employed. This method allows for the identification of weak interactions by analyzing regions of low electron density and their corresponding gradient. The interaction strength and types are interpreted using the product of electron density, $\rho(r)$, and the second eigenvalue (λ_2) of the Hessian matrix of $\rho(r)$. The RDG function is defined by the following equation:[56]

$$\text{RDG}(r) = \frac{1}{2(3\pi^2)^{\frac{1}{3}}} \frac{|\nabla\rho(r)|}{\rho(r)^{\frac{3}{4}}} \quad (3)$$

Here, $\nabla\rho(r)$ represents the gradient of the electron density, and $\rho(r)$ is the electron density at a point r. This analysis is used for qualitative identification and characterization of several weak interactions, such as steric repulsion, hydrogen bonding, and van der Waals forces. The RDG and NCI analyses were conducted using the Multiwfn software package,[57] while the resulting isosurfaces were visualized using Visual Molecular Dynamics (VMD).[58]

An eight-unit thiophene oligomer, the PTh octamer, is widely considered an appropriate model for replicating the electronic characteristics of the PTh polymer.[59,60] The relaxed geometry of PTh is represented in Fig. 1. The calculated band gaps for PTh (2.63 eV) using DFT studies in this work are in good agreement with the experimental data (≈2.0–2.3 eV), thereby supporting the accuracy and reliability of the computational protocol and inferences drawn from this work.[61,62]

3. Results and discussion

3.1 Properties of TM@PTh complexes

The spin-polarized DFT calculations were performed to identify the most stable spin states for TM@PTh complexes. This step was crucial for examining transition metals (TMs) as their valence electrons occupy partially filled d-orbitals, making electron pairing and magnetic properties highly sensitive to the surrounding electronic environment. The spin state of a TM complex was defined by its spin multiplicity, $S = 2s + 1$, where s denotes the total spin. For example, Scandium (Sc) and Cobalt (Co) showed doublet and quartet states, while titanium (Ti) and iron (Fe) exhibited singlet, triplet, and quintet multiplicities. Vanadium(v) and manganese (Mn) showed doublet, quartet, and sextet states, whereas Chromium (Cr) exhibited singlet, triplet, quintet, and septet states. In contrast, nickel (Ni) was limited to singlet and triplet spin states, and copper (Cu), with a single unpaired electron, exhibited only the doublet state. Zinc (Zn) with all electrons paired exhibited only the singlet state. These optimized spin states were used in subsequent calculations to ensure accurate modeling of the TM@PTh systems.

Fig. 2 represents a comparative analysis of the relative energies corresponding to different spin states of TM@PTh complexes. The most stable and energetically favourable spin states were identified as doublet for Sc@PTh, quartet for

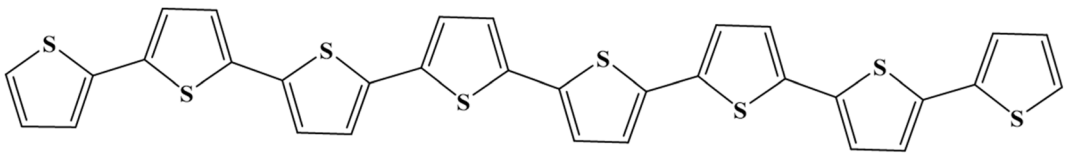

Fig. 1 Chemical structure of the polythiophene (PTh) backbone used as a sensing substrate for transition-metal (TM) decoration (TM@PTh).

 © 2026 The Author(s). Published by the Royal Society of Chemistry

Open Access Article. Published on 02 March 2026. Downloaded on 3/21/2026 1:02:11 PM.
This article is licensed under a Creative Commons Attribution-NonCommercial 3.0 Unported Licence.

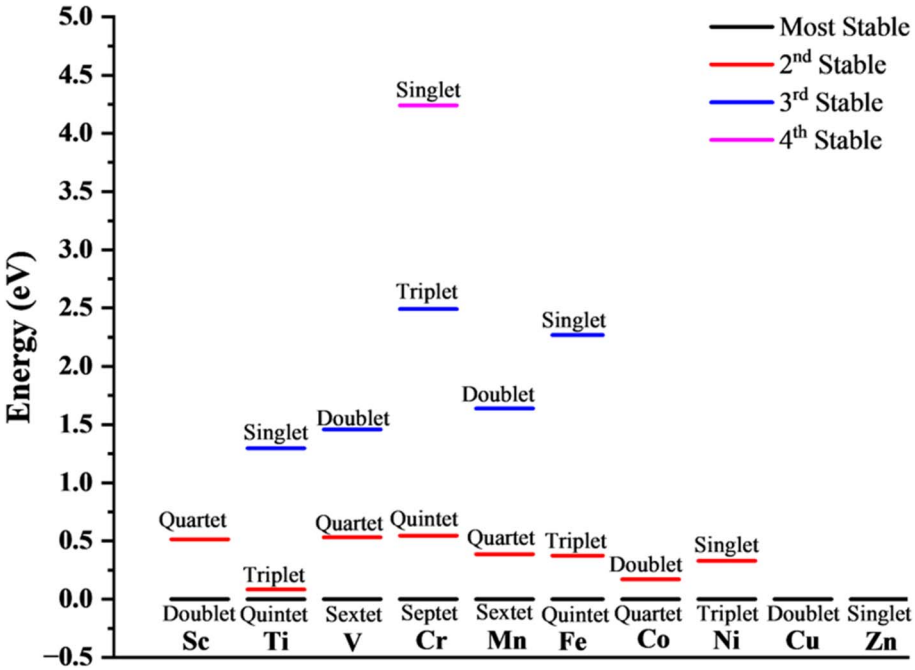

Fig. 2 Comparison of relative energies (eV) for different spin states of TM@PTh composites.

Co@PTh, and quintet for Ti@PTh and Fe@PTh. For the V@PTh and Mn@PTh composites, the sextet spin state was found to be most stable among other considered spin states. Notably, Cr@PTh and Ni@PTh composites were most stable in the septet and triplet states, respectively. These variations highlighted the critical importance of spin-polarized calculations in accurately determining the ground-state electronic configuration of various TM composites. For instance, the energy gap between the septet and singlet states of Cr@PTh was as large as 4.24 eV. This significant energy gap could be attributed to the inherent stability of half-filled d-orbitals, a well-established concept in transition metal chemistry, where half-filled and filled electronic configurations confer greater thermodynamic stability than other electronic arrangements.

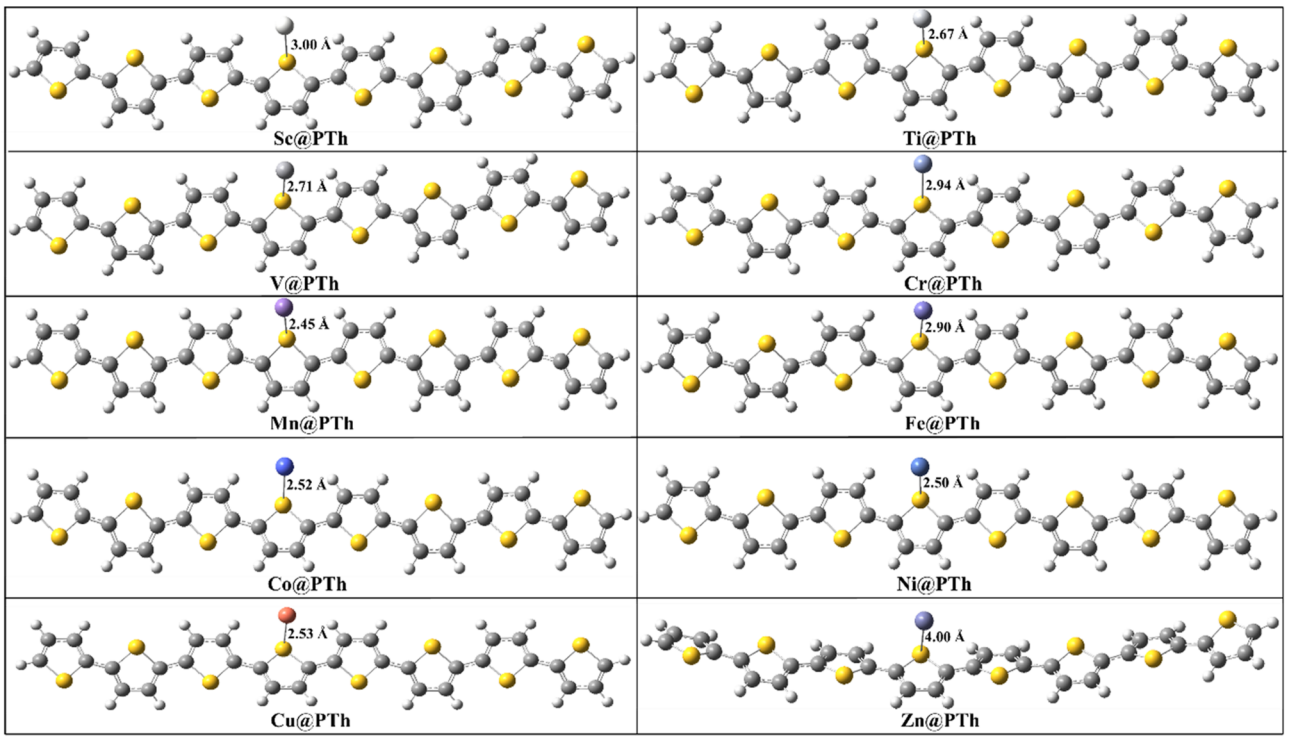

Fig. 3 Optimized structures of the most stable spin state of various TM@PTh composites.

Open Access Article. Published on 02 March 2026. Downloaded on 3/21/2026 1:02:11 PM.
This article is licensed under a Creative Commons Attribution-NonCommercial 3.0 Unported Licence.

Fig. 3 depicts the relaxed structures of TM@PTh composites corresponding to the most stable spin states, highlighting the bond lengths between the sulfur (S) atom of the PTh backbone and the TM atoms ($d_{S2\text{-}TM4}$). For most TM@PTh composites, $d_{S2\text{-}TM4}$ values fall within the range of 2.45 to 3.00 Å, indicating moderate binding interactions between the polymer and the metal center. An exception is observed for Zn@PTh, which exhibits a significantly longer bond length of 4.00 Å, suggesting weak non-covalent interactions due to the filled d^{10} configuration of Zn. Additional structural parameters, *i.e.*, the $\angle C_1S_2C_3$ bond angle, refer to the angle formed between two carbon atoms (C_1 and C_2) and the intervening S_2 atom in the PTh backbone. This angle is a key structural parameter that reflects the planarity and conjugation within the thiophene ring system. The values of $d_{S2\text{-}TM4}$ bond lengths and the $\angle C_1S_2C_3$ bond angles are summarized in Table 1. Deviations in bond angle ($\Delta\angle C_1S_2C_3$) are computed relative to the pristine PTh of 92.05°, providing a measure of angular distortion upon TM coordination. Sc@PTh (doublet state) shows $d_{S2\text{-}TM4}$ of 3.00 Å and the slight increase in angle to 92.25°, corresponding to $\Delta = -0.20°$.

Table 1 Optimized structural parameters for various spin states of TM@PTh composites, including bond lengths between the sulfur (S) atom of the PTh backbone and the TM atoms ($d_{S2\text{-}TM4}$), bond angles formed between the two carbon atoms (C_1 and C_3) and the intervening sulfur atom (S_2) in the PTh backbone ($\angle C_1S_2C_3$) and deviation in the bond angle relative to the bare PTh system ($\Delta\angle C_1S_2C_3$)

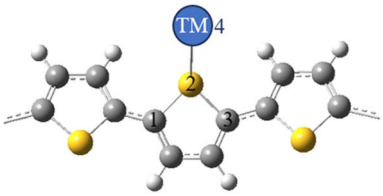

System	Spin state	$d_{S2\text{-}TM4}$ (Å)	$\angle C_1S_2C_3$ (deg)	$\Delta\angle C_1S_2C_3$ (deg)
PTh			92.05	
Sc@PTh	Doublet	3.00	92.25	−0.20
Ti@PTh	Singlet	2.25	90.94	1.11
	Triplet	2.75	92.27	−0.22
	Quintet	2.67	92.18	−0.13
V@PTh	Doublet	2.62	92.12	−0.07
	Quartet	2.66	92.25	−0.20
	Sextet	2.71	92.08	−0.03
Cr@PTh	Singlet	2.25	91.70	0.35
	Triplet	2.36	91.22	0.83
	Quintet	2.61	92.29	−0.24
	Septet	2.94	92.23	−0.18
Mn@PTh	Doublet	2.38	91.78	0.27
	Quartet	2.34	91.08	0.97
	Sextet	2.45	91.09	2.74
Fe@PTh	Singlet	2.13	91.42	0.63
	Triplet	2.44	92.00	0.05
	Quintet	2.90	92.21	−0.16
Co@PTh	Doublet	2.42	92.14	−0.09
	Quartet	2.52	92.19	−0.14
Ni@PTh	Singlet	2.03	91.35	0.70
	Triplet	2.46	92.24	−0.19
Cu@PTh	Doublet	2.53	92.27	−0.22
Zn@PTh	Singlet	4.00	92.12	−0.07

In Ti@PTh, the singlet state shows a notably shorter bond length of 2.25 Å and a larger angular contraction to 90.94° ($\Delta\angle C_1S_2C_3 = +1.11°$), while the higher spin states (triplet and quintet) exhibit longer bond lengths (2.75 and 2.67 Å) and bond angles closer to the reference geometry, *i.e.*, 92.27° and 92.18°, respectively.

V@PTh and Cr@PTh exhibit minimal angular deviations across their respective spin states. For V@PTh, $\Delta\angle C_1S_2C_3$ values range from −0.07° (doublet) to −0.20° (quartet), with a maximum deviation of −0.03° observed in the sextet state. Cr@PTh displays slightly more pronounced distortions, with $\Delta\angle C_1S_2C_3$ values ranging from +0.35° (singlet) and +0.83° (triplet) to −0.24°(quintet) and −0.18°(septet). Mn@PTh displays a clear spin-dependent trend, where the sextet state produces the greatest deviation ($\Delta\angle C_1S_2C_3 = +2.74°$), indicating increased angular strain. Fe@PTh is accompanied by relatively smaller angular changes ($\Delta\angle C_1S_2C_3 = +0.63°$ in the singlet to −0.16° in the quintet). Co@PTh and Ni@PTh display minimal deviations in bond angle, suggesting stable geometries across spin states ($\Delta\angle C_1S_2C_3$ ranging from −0.14° to −0.09° for Co, and +0.70° to −0.19° for Ni). Cu@PTh exhibits minimal deviation for the $\Delta\angle C_1S_2C_3 = -0.22°$, while Zn@PTh, shows negligible angular distortion ($\Delta\angle C_1S_2C_3 = -0.07°$).

Overall, these results suggest that most TMs induce minor geometric perturbation in the PTh backbone ($|\Delta\angle C_1S_2C_3| < 1°$), except high-spin Mn@PTh. Furthermore, $d_{S2\text{-}TM4}$ tends to increase with spin multiplicity, reflecting the interplay between TM-sulfur bonding and electron–electron repulsion within the TM center.

Table 2 summarizes the binding energies (E_{bin}) of all TM@PTh composites across different spin states. Notably, the most stable configurations for each composite are observed to be associated with the highest spin multiplicity of the transition metal, highlighting the importance of spin state optimization in stability. Among all the systems, Cr@PTh exhibits the highest binding energy ($E_{bin} = -5.37$ eV), indicating the strongest interaction with the PTh matrix, followed by Fe@PTh and Mn@PTh. In contrast, Zn@PTh shows the lowest binding energy due to its filled $3d^{10}$ electron configuration, which limits its stability to interact with the polymer. It is thus excluded from further studies due to its negligible binding energy. The binding energies and the composite stability show the following order: Cr@PTh (−5.37 eV) > Fe@PTh (−3.47 eV) > Mn@PTh (−2.76 eV) > V@PTh (−2.44 eV) > Ti@PTh (−1.90 eV) > Ni@PTh (−1.81 eV) > Sc@PTh (−1.16 eV) > Co@PTh ≈ Cu@PTh (−0.20 eV) > Zn@PTh (−0.01 eV).

It is well documented in the literature that $E_{bin} > 1$ eV is characteristic of chemisorption, indicating strong and stable chemical bonding among the species involved.[63,64] In the present study, all the TM@PTh composites except Co@PTh, Cu@PTh, and Zn@PTh have the E_{bin} values exhibiting this threshold value, thereby implying robust chemical attachment of the TM centers and the PTh polymer.

To quantitatively evaluate charge distribution upon metal adsorption, Natural Bond Order (NBO) partial atomic charges were computed for all TM@PTh complexes. The computed partial atomic charges reveal that most TMs carry a positive

 © 2026 The Author(s). Published by the Royal Society of Chemistry

Open Access Article. Published on 02 March 2026. Downloaded on 3/21/2026 1:02:11 PM.
This article is licensed under a Creative Commons Attribution-NonCommercial 3.0 Unported Licence.

Table 2 Binding energies (E_{bin}), energies of the highest occupied molecular (E_{HOMO}) and lowest unoccupied molecular orbital (E_{LUMO}), energy gap between HOMO and LUMO (E_{gap}), and dipole moment (μ) of various TM@PTh composites. The most stable states of each composite are highlighted in bold

System	Spin state	E_{bin} (eV)	E_{HOMO} (eV)	E_{LUMO} (eV)	E_{gap} (eV)	μ (D)
PTh	—	—	−5.05	−2.42	2.63	1.17
Sc@PTh	Doublet	−1.16	−4.11	−2.71	1.40	2.61
Ti@PTh	Singlet	−0.60	−4.02	−2.55	1.47	1.38
	Triplet	−1.81	−4.43	−2.76	1.67	1.86
	Quintet	**−1.90**	**−3.75**	**−2.53**	**1.22**	**1.17**
V@PTh	Doublet	−0.98	−4.53	−2.75	1.79	1.95
	Quartet	−1.91	−4.69	−2.79	1.90	1.57
	Sextet	**−2.44**	**−3.74**	**−2.60**	**1.14**	**1.34**
Cr@PTh	Singlet	−1.13	−4.00	−2.66	1.34	1.47
	Triplet	−2.88	−5.08	−2.64	2.44	1.78
	Quintet	−4.82	−4.96	−2.87	2.09	0.53
	Septet	**−5.37**	**−4.07**	**−2.52**	**1.55**	**1.50**
Mn@PTh	Doublet	−1.12	−5.08	−2.71	2.37	2.08
	Quartet	−2.37	−5.09	−2.72	2.37	1.94
	Sextet	**−2.76**	**−4.31**	**−2.46**	**1.85**	**1.71**
Fe@PTh	Singlet	−0.83	−4.19	−2.67	1.52	1.74
	Triplet	−3.09	−5.05	−2.82	2.23	1.78
	Quintet	**−3.47**	**−4.66**	**−2.58**	**2.08**	**2.34**
Co@PTh	Doublet	−0.33	−5.07	−2.80	2.27	1.91
	Quartet	**−0.20**	**−4.24**	**−2.55**	**1.69**	**1.79**
Ni@PTh	Singlet	−1.48	−4.52	−2.54	1.98	0.71
	Triplet	**−1.81**	**−4.28**	**−2.56**	**1.72**	**2.05**
Cu@PTh	Doublet	−0.20	−4.31	−2.53	1.78	1.85
Zn@PTh	Singlet	−0.01	−5.07	−2.44	2.63	1.54

charge upon incorporation into the polymer matrix, indicating net electron donation from the metal to the π-conjugated framework.[65,66] Specifically, the NBO charges are +0.038e (Sc), +0.118e (Ti), +0.081e (V), +0.064e (Cr), +0.155e (Mn), +0.057e (Co), +0.028e (Ni), and +0.031e (Cu). The magnitude of charge transfer is most pronounced for Ti and Mn, suggesting strong metal-to-polymer electron donation in these systems. In contrast, Fe (−0.017e) and Zn (−0.006e) indicate minimal net charge transfer and a more covalent interaction character. The magnitude of charge transfer correlates with the observed variation in HOMO–LUMO gaps, confirming that metal-to-polymer electron donation plays a key role in tuning the electronic structure of TM@PTh composites.

Consistent with this charge redistribution, the frontier molecular orbital (FMO) energy levels corresponding to the most stable spin configuration of TM@PTh complexes are provided in Fig. 4. HOMO and LUMO for the bare PTh and the most stable spin states for TM@PTh are shown in Fig. 5. For bare PTh, both the HOMO and LUMO orbitals are delocalized along the π-conjugated polymer backbone, indicative of a typical conjugated system. The incorporation of transition metal atoms results in a significant redistribution of the frontier orbitals. In most TM@PTh composites, the HOMO is localized around the TM centers, suggesting strong orbital hybridization and possible charge donation from the metal to PTh polymer. The LUMO orbitals, in contrast, remain largely delocalized along the polymer chain. These changes in orbital distribution reflect modified electronic properties induced by TM incorporation, which may impact charge transport, sensing response, and catalytic activity. To gain deeper insight into the modifications in the electronic structure, the spin-resolved density of states (DOS) spectra for the system under consideration are shown in Fig. S1(a–j). For all the systems, pronounced states are observed near the Fermi level, indicating the involvement of metal-derived d-orbitals in frontier energy regions. Compared to bare PTh, the introduction of TM atoms generates additional electronic states within the band gap region and enhances the DOS around the HOMO level. This behavior confirms strong metal-polymer orbital interactions. The narrowing or broadening of the energy gap observed in the DOS plots is consistent with the calculated HOMO–LUMO gaps, supporting the reliability of the FMO analysis.

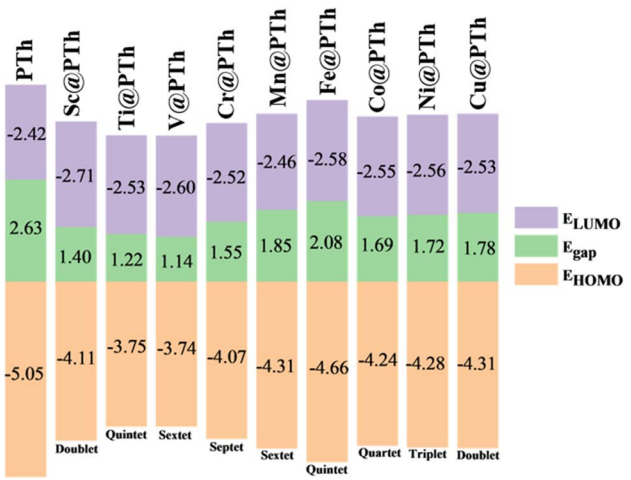

Fig. 4 The frontier molecular orbital (FMO) energy levels of PTh and the most stable spin configuration of TM@PTh complexes.

Open Access Article. Published on 02 March 2026. Downloaded on 3/21/2026 1:02:11 PM.
This article is licensed under a Creative Commons Attribution-NonCommercial 3.0 Unported Licence.

Complex	HOMO	LUMO
PTh	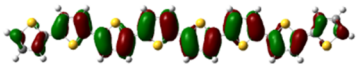	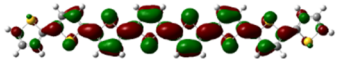
Sc@PTH	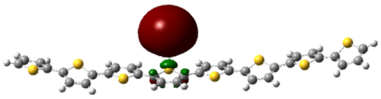	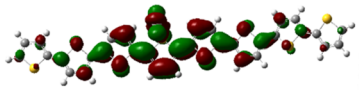
Ti@PTh	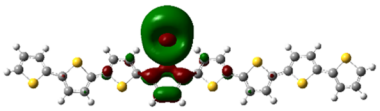	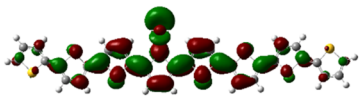
V@PTh	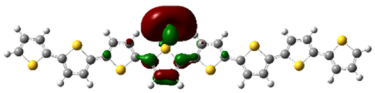	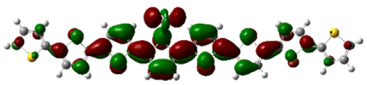
Cr@PTh	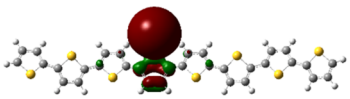	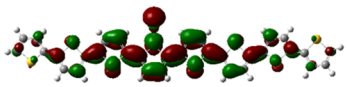
Mn@PTh	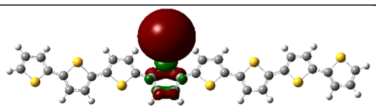	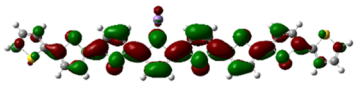
Fe@PTh	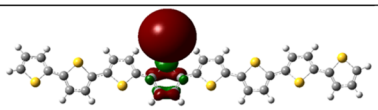	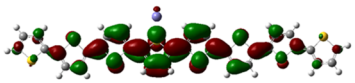
Co@PTh	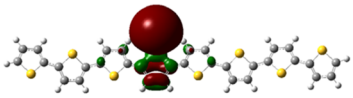	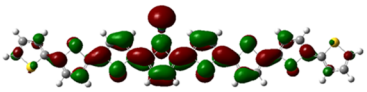
Ni@PTh	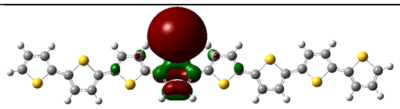	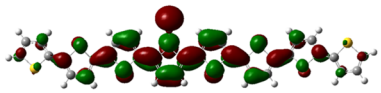
Cu@PTh	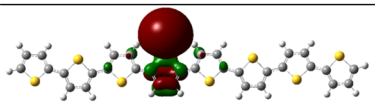	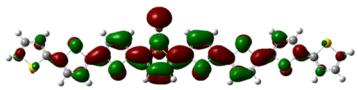

Fig. 5 HOMO and LUMO electron distribution plot of the pristine PTh and the most stable spin states of TM@PTh composites.

Consistent with these DOS features, the computed HOMO–LUMO energy gap (E_{gap}) and dipole moment (μ) were calculated for each system to assess the chemical stability, electronic reactivity, and charge distribution. Upon incorporation of TM, significant variations in both the energy gap and dipole moment were observed depending on the nature of the

 © 2026 The Author(s). Published by the Royal Society of Chemistry

Open Access Article. Published on 02 March 2026. Downloaded on 3/21/2026 1:02:11 PM.
This article is licensed under a Creative Commons Attribution-NonCommercial 3.0 Unported Licence.

transition metal and spin state. For instance, Sc@PTh (doublet) shows a reduced energy gap of 1.40 eV and a higher dipole moment of 2.61 D, indicating enhanced electronic reactivity. Ti@PTh displays spin-dependent electronic behavior, with singlet, triplet, and quintet states exhibiting energy gaps of 1.47, 1.67, and 1.22 eV, respectively, and corresponding dipole moments ranging from 1.17 to 1.86 D. V@PTh exhibits a narrow gap of 1.14 eV and a moderate dipole moment of 1.34 D for the sextet state. Cr@PTh exhibits a wide energy gap from 1.34 eV for the singlet state to 2.44 eV for the triplet, with dipole moments of 0.53 and 1.78 D, respectively. Notably, doublet and quartet states of Mn@PTh exhibit relatively higher energy gaps of 2.37 eV with dipole moments of 2.08 and 1.94 D, respectively, indicating enhanced stability across spin states. Fe@PTh also shows moderate to high energy gaps of 1.52 to 2.23 eV, with the quintet state displaying a dipole moment of 2.34 D. Co@PTh and Ni@PTh exhibit spin-dependent behavior with E_{gap} ranging from 1.69 to 2.27 eV and dipole moments varying between 0.71 and 2.05 D. Cu@PTh (doublet) has moderate E_{gap} of 1.78 eV and dipole moment of 1.85 D. In contrast, Zn@PTh (singlet), consistent with its filled shell configuration, exhibits the widest E_{gap} of 2.63 eV and a moderate dipole moment of 1.54 D, reflecting its closed-shell electronic stability. Overall, the combined FMO and DOS analyses demonstrate that incorporation of transition metal atoms enables effective tuning of the electronic structure of TM@PTh composites. The modulation of energy levels, spin polarization, and charge distribution plays a crucial role in determining their suitability for applications in optoelectronics, sensing, and catalysis.

To evaluate the type and magnitude of non-covalent interactions (NCI) among different TM@PTh composites, both 3D isosurfaces and 2D scatter plots of RDG *versus* (sign λ_2) ρ were generated for the most stable spin configuration of TM@PTh complexes, as illustrated in Fig. 6 and 7, respectively. In NCI analysis, the repulsive (non-bonded) forces are typically represented by positive values ((sign $\lambda_2)\rho > 0$), attractive interactions by negative values ((sign $\lambda_2)\rho < 0$), and van der Waals (vdW) (weak dispersive) forces by (sign $\lambda_2)\rho \approx 0$. These interactions are visually encoded in the plots using the following color conventions: blue signifies strong electrostatic attractions, red indicates steric repulsion, and green represents dispersion forces. The 3D isosurfaces and corresponding RDG scatter plots reveal a prominent green region between the TM atoms and the hydrogen atom of the PTh chain, as well as green spikes near −0.01 a.u., indicating dominant dispersive interactions. Notably, Sc@PTh, Ti@PTh, V@PTh, Cr@PTh, Mn@PTh, Co@PTh, Ni@PTh, and Cu@PTh reveal more pronounced blue–green regions near the metal–sulfur coordination site, suggesting stronger localized attractive interactions with partial covalent character arising from d–π orbital hybridization. In contrast, Fe@PTh and Zn@PTh exhibit weaker, more diffuse attractive regions, consistent with their minimal net charge transfer and relatively weaker electronic perturbations. Red isosurfaces are clearly visible within the aromatic rings of the polymer backbone across all systems, reflecting steric repulsion and intrinsic ring strain associated with the π-conjugated framework. Importantly, while the internal ring repulsion remains largely unchanged upon doping, the intensity and

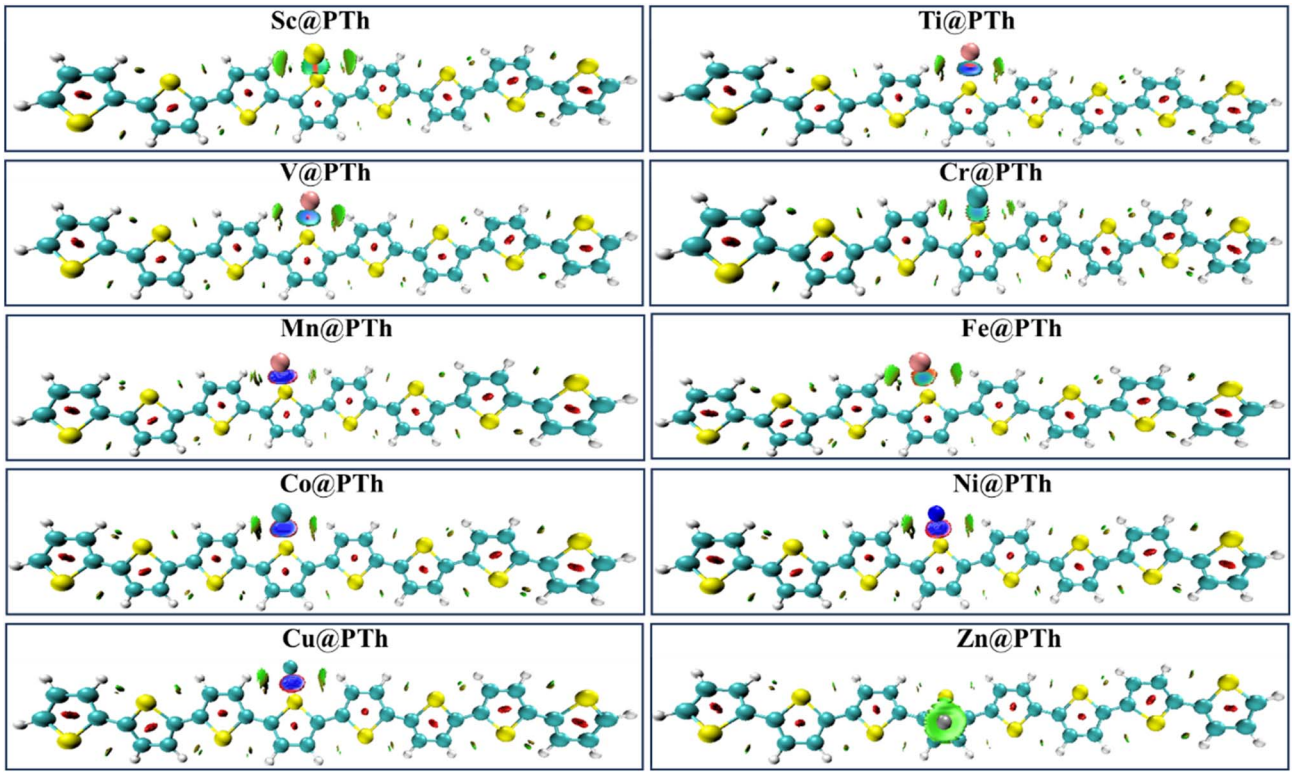

Fig. 6 Non-covalent interaction (NCI) analysis through 3D isosurfaces of the most stable spin state of TM@PTh complexes.

Open Access Article. Published on 02 March 2026. Downloaded on 3/21/2026 1:02:11 PM.
This article is licensed under a Creative Commons Attribution-NonCommercial 3.0 Unported Licence.

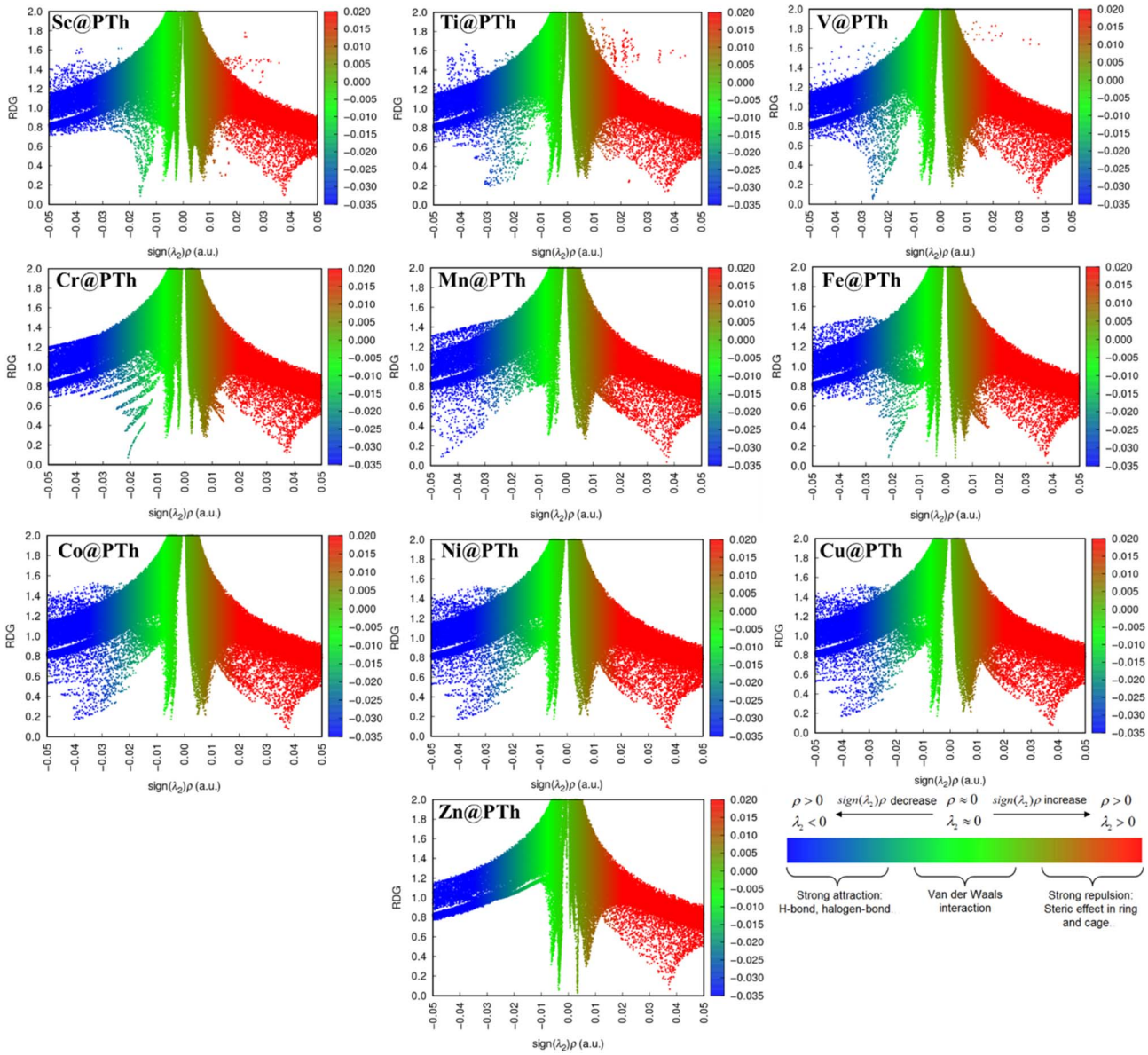

Fig. 7 Non-covalent interaction (NCI) analysis through 2D reduced density gradient (RDG) spectra of the most stable spin state of TM@PTh complexes. The red, blue, and green regions indicate steric repulsion, strong attractive interactions, and weak vdW interactions, respectively.

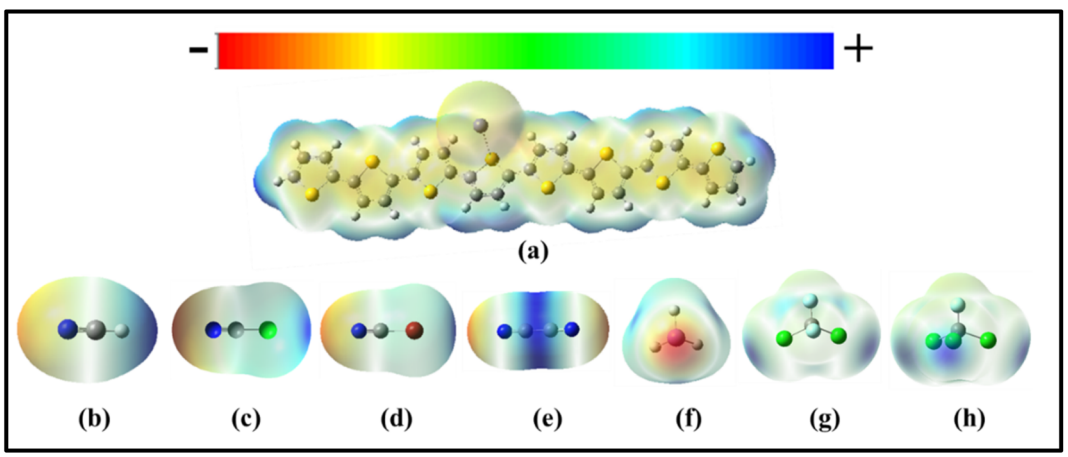

Fig. 8 Molecular electrostatic potential (MEP) plots for (a) Fe@PTh, (b) HCN, (c) NCCl, (d) NCBr, (e) NCCN, (f) AsH_3, (g) CFC-11, and (h) CFC-12.

 © 2026 The Author(s). Published by the Royal Society of Chemistry

Open Access Article. Published on 02 March 2026. Downloaded on 3/21/2026 1:02:11 PM.
This article is licensed under a Creative Commons Attribution-NonCommercial 3.0 Unported Licence.

spatial extent of the green and blue regions around the coordination site vary depending on the transition metal. Complexes exhibiting broader dispersion regions and more intense attractive features correspond to stronger stabilization, correlating well with their computed binding energies.

Overall, the comparative NCI analysis demonstrates that TM adsorption is governed by a synergistic interplay of dispersion forces, electrostatic attraction, and orbital hybridization effects, rather than purely covalent bonding, thereby rationalizing the stability trends observed for the TM@PTh composites.

Due to their abundance and lower toxicity, TM@PTh composites offer a cost-effective and sustainable alternative for sensing harmful pollutants. Although Cr@PTh exhibits high binding energy and the lowest HOMO–LUMO gap (E_{gap}) (as

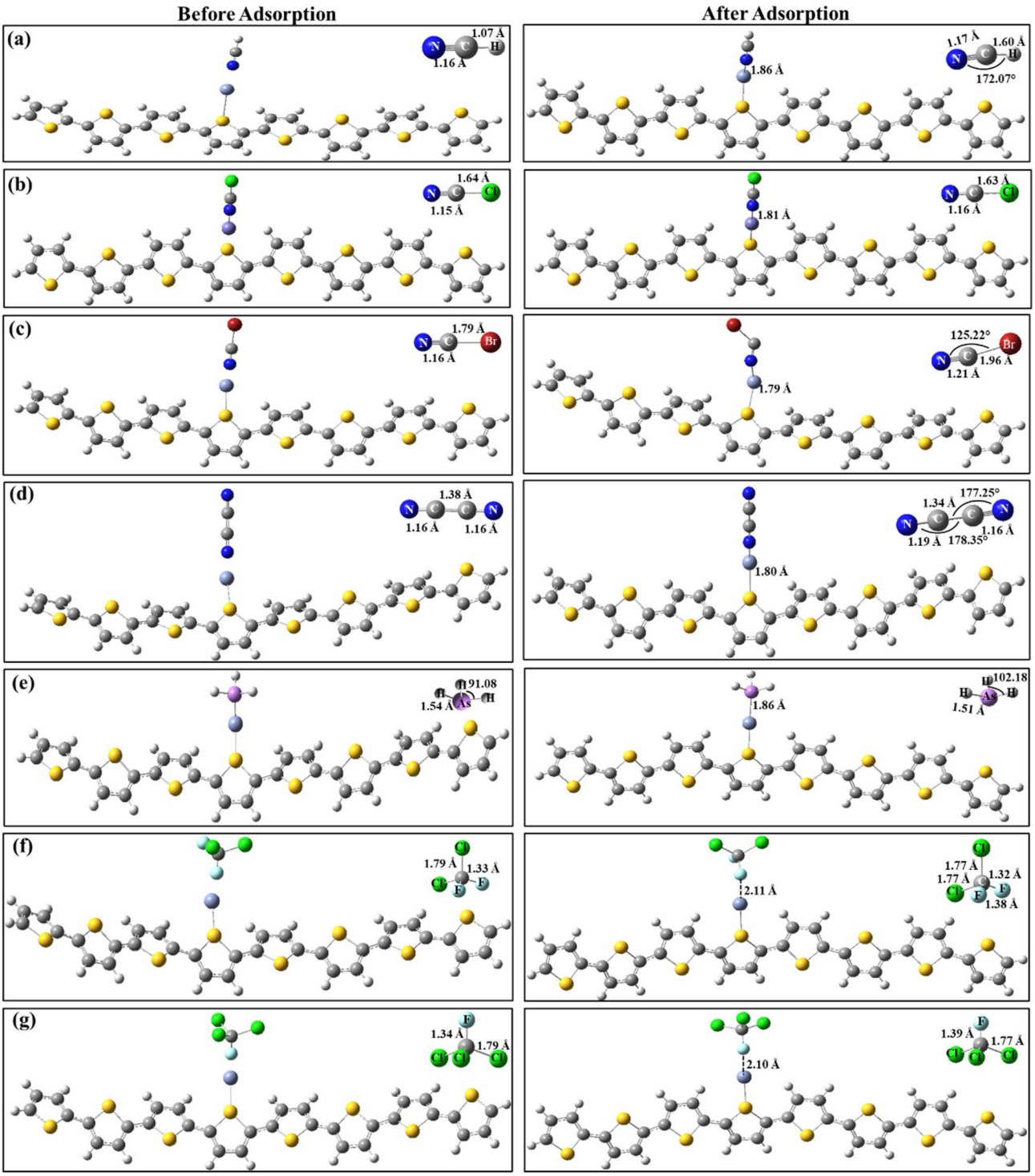

Fig. 9 Optimized geometries of Fe@PTh-analyte complexes: (a) HCN, (b) NCCl, (c) NCBr, (d) NCCN, (e) AsH_3, (f) CFC-11, and (g) CFC-12, alongside the pristine structures of CWAs and CFCs.

Open Access Article. Published on 02 March 2026. Downloaded on 3/21/2026 1:02:11 PM.
This article is licensed under a Creative Commons Attribution-NonCommercial 3.0 Unported Licence.

evident from Table 2), its low energy gap may restrict its suitability as a sensing material for the considered analytes. Given the high binding energy and the largest E_{gap}, Fe@PTh indicates potential to be examined further for analyzing its ability to sense hazardous substances such as chemical warfare agents (CWAs) and chlorofluorocarbons (CFCs).

3.2 Sensitivity of Fe@PTh composite in detecting chemical warfare agents and chlorofluorocarbons

To assess the sensing capability of TM@PTh composites towards chemical warfare agents (CWAs) and chlorofluorocarbons (CFCs), representative analytes from each category were selected for investigation. Among CWAs, HCN, NCCl, NCBr, NCCN, and AsH_3, were chosen owing to their high toxicity, rapid physiological effects, and environmental persistence, making them highly dangerous even at trace levels. On the other hand, CFC-11 and CFC-12 were selected due to their exceptional atmospheric stability and well-documented role in ozone layer depletion.[38–40] Together, these analytes represent a chemically diverse and environmentally significant set of analytes providing a robust framework to evaluate their sensitivity, selectivity, and applicability of TM@PTh composites for toxic gas detection.

The molecular electrostatic potential (MEP) plots were first analyzed to identify the most reactive sites of each species (Fig. 8). The MEP plots use a color-coded scale, where red indicates electron-rich regions, blue denotes electron-deficient regions, and green corresponds to areas with neutral potential. As indicated in Fig. 8, the electrostatic surface of Fe@PTh reveals a region surrounding the Fe atom that exhibits relatively less negative (or comparatively positive) potential than the neighboring heteroatom-rich regions, making it a favorable site for interaction with electronegative atoms.

For CWAs such as HCN, NCCl, NCBr, NCCN, and AsH_3, the most electronegative regions are located around the nitrogen or arsenic atoms. In contrast, for CFC-11 and CFC-12, the regions of highest electronegativity are primarily localized around the halogen atoms (F and Cl). Consequently, in all Fe@PTh–analyte complexes, the interactions predominantly occur between the electropositive Fe center in Fe@PTh and the electronegative atoms of the CWAs and CFCs.

The optimized geometries of all Fe@PTh–analyte complexes, shown in Fig. 9, depict intermolecular bond distances ranging from 1.79 to 2.11 Å, indicating strong and specific interactions. Additionally, the CWAs and CFCs undergo significant structural distortions upon interaction with the Fe@PTh composite, including alterations in bond lengths and angles (Fig. 9). These structural perturbations in CWAs and CFCs induced by binding with Fe@PTh influence the electronic properties of the complexes, as revealed by the shifts in HOMO and LUMO energy levels, leading to a reduced HOMO–LUMO energy gap (E_{gap}). Compared to the pristine Fe@PTh system with $E_{gap} = 2.08$ eV, complexation with the analyte results in decreased energy gaps: 1.67 eV for Fe@PTh–HCN, 1.69 eV for Fe@PTh–NCCl, 1.69 eV for Fe@PTh–NCBr, 2.03 eV for Fe@PTh–NCCN, 1.86 eV for Fe@PTh–AsH_3, 1.76 eV for Fe@PTh–CFC-11, and 1.80 eV for Fe@PTh–CFC-12. The most pronounced reductions in E_{gap} are observed for the Fe@PTh–HCN and Fe@PTh–CFC-11 complexes, primarily driven by upward shifts in HOMO energy levels (see Table 3).

This trend is further supported by DOS analyses (Fig. S1), which show enhanced orbital overlaps in the Fe@PTh and the adsorbed analytes, indicating strong electronic interactions. The computed interaction energies (E_{int}) further validate these findings with particularly strong binding observed for Fe@PTh–NCCN (−44.79 kcal mol^{-1}), Fe@PTh–HCN (−35.28 kcal mol^{-1}), and Fe@PTh–ClCN (−34.01 kcal mol^{-1}). In contrast, CFCs exhibit comparatively weaker interactions with E_{int} values of −4.72 kcal mol^{-1} (CFC-11) and −4.97 kcal mol^{-1} (CFC-12). Despite their lower binding affinities, CFCs induce measurable perturbations in the electronic and dipolar properties of the Fe@PTh composite. These results indicate that Fe@PTh is not only sensitive to reactive CWAs but also capable of detecting environmentally persistent CFCs by observing noticeable modifications in the electronic structure.

Evaluating charge transfer is essential for a thorough understanding of the electronic properties and interaction mechanism between the composite and the investigated analytes. To quantify this effect, NBO analysis was performed to determine the magnitude and direction of electron transfer during the interaction of the CWAs/CFCs with the composite.[67] The amount of charge transfer (q, in e) was calculated as the difference between the total NBO charge on the CWA/CFC molecules before adsorption and after complex formation. The calculated NBO charges are summarized in Table 3. The results show that electron density is generally transferred from the composite to the CWAs/CFCs. However, in the case of AsH_3

Table 3 Interaction energies (E_{int}), energies of the highest occupied molecular (E_{HOMO}) and lowest unoccupied molecular orbital (E_{LUMO}), energy gap between HOMO and LUMO (E_{gap}), dipole moment (μ), and extent of charge transfer (q) of Fe@PTh–analyte systems

System	E_{int} (kcal mol^{-1})	E_{HOMO} (eV)	E_{LUMO} (eV)	E_{gap} (eV)	μ (D)	q (e)
Fe@PTh		−4.66	−2.58	2.08	2.34	
Fe@PTh-HCN	−35.28	−4.15	−2.48	1.67	1.52	0.009
Fe@PTh-NCCl	−34.01	−4.15	−2.46	1.69	1.53	0.003
Fe@PTh-NCBr	−2.37	−4.15	−2.46	1.69	1.97	0.060
Fe@PTh-NCCN	−44.79	−4.78	−2.75	2.03	6.29	0.204
Fe@PTh-AsH_3	−26.21	−4.29	−2.43	1.86	1.79	−0.161
Fe@PTh-CFC-11	−4.72	−4.18	−2.42	1.76	2.94	0.508
Fe@PTh-CFC-12	−4.97	−4.20	−2.40	1.80	2.36	−0.078

 © 2026 The Author(s). Published by the Royal Society of Chemistry

Open Access Article. Published on 02 March 2026. Downloaded on 3/21/2026 1:02:11 PM.
This article is licensed under a Creative Commons Attribution-NonCommercial 3.0 Unported Licence.

and CFC-12, the direction of charge transfer is reversed, with electron density flowing from AsH_3 and CFC-12 to the composite.

4. Conclusions

The present study examines the potential application of the first-row transition metal (Sc → Zn) based polythiophene (TM@PTh) composites for the detection of CWAs and CFCs using DFT analysis. The structural and electronic properties of TM@PTh composites were systematically investigated across multiple spin configurations. Spin-polarized calculations revealed that these composites are most stable in their highest spin multiplicities. Among all candidates, Cr@PTh (septet) and Fe@PTh (quintet) exhibited the greatest thermodynamic stability, with binding energies of −5.37 eV and −3.47 eV, respectively. Although Cr@PTh shows the highest binding energy, its narrow HOMO–LUMO gap (E_{gap}), may limit its suitability for sensing performance. In contrast, Fe@PTh exhibited an optimal combination of high thermodynamic stability, large E_{gap}, and high binding energies with the target analytes, identifying it as the most promising candidate for further studies. To elucidate the nature of intermolecular interactions, RDG analysis was performed using 3D isosurface visualizations and 2D scatter plots of RDG *versus* (sign λ_2)ρ. The calculated interaction energies (E_{int}), ranging from −2.37 to −44.79 kcal mol^{-1}, conform to the strong binding of Fe@PTh composite with both highly reactive chemical warfare agents and environmentally stable chlorofluorocarbons, accompanied by significant perturbations in the electronic structure upon adsorption. From an experimental standpoint, these adsorption-induced electronic perturbations suggest that Fe@PTh-based sensors may exhibit low detection limits and high sensitivity toward the investigated analytes. The moderate yet stable interaction strengths further imply the possibility of rapid response and recovery times, along with good reversibility during repeated sensing cycles. Overall, these findings highlight Fe@PTh as a promising sensing material, providing a theoretical basis for future experimental validation and extension to other polymer-metal sensing systems.

Conflicts of interest

The authors declare no competing interests.

Data availability

The data will be made available by authors on request.

Supplementary information (SI): density of state (DOS) plot analysis of most stable spin state of the TM@PTh hybrid from Sc to Zn. See DOI: https://doi.org/10.1039/d6ra00636a.

Acknowledgements

SY thanks the Indian Institute of Technology (Indian School of Mines) (IIT(ISM)) Dhanbad for the Postdoctoral grant and for providing the facility to work. The authors thank the HPC facility of IIT(ISM) Dhanbad.

References

1 R. Gangopadhyay and A. De, Conducting Polymer Nanocomposites: A Brief Overview, *Chem. Mater.*, 2000, **12**(3), 608–622, DOI: 10.1021/cm990537f.
2 Z.-F. Li, F. D. Blum, M. F. Bertino and C.-S. Kim, Amplified Response and Enhanced Selectivity of Metal-PANI Fiber Composite Based Vapor Sensors, *Sens. Actuators, B*, 2012, **161**(1), 390–395.
3 S. Garg and N. Goel, First Principle Study of Hybrid Materials Based on Conjugated Polymers and Zirconium Oxide as a Proficient Sensor for H_2S Gas, *Mol. Phys.*, 2022, e2150332, DOI: 10.1080/00268976.2022.2150332.
4 M. Y. Lo, C. Zhen, M. Lauters, G. E. Jabbour and A. Sellinger, Organic−Inorganic Hybrids Based on Pyrene Functionalized Octavinylsilsesquioxane Cores for Application in OLEDs, *J. Am. Chem. Soc.*, 2007, **129**(18), 5808–5809, DOI: 10.1021/ja070471m.
5 S. Garg and N. Goel, Photodegradation of Dye Using Polythiophene/ZnO Nanocomposite: A Computational Approach, *J. Mol. Graphics Modell.*, 2022, **117**, 108285.
6 B. K. Mallick, M. Witcomb and M. Scurrell, Palladium-Polyaniline and Palladium-Polyaniline Derivative Composite Materials, *Platinum Met. Rev.*, 2007, **51**(1), 3–15.
7 B. J. Gallon, R. W. Kojima, R. B. Kaner and P. L. Diaconescu, Palladium Nanoparticles Supported on Polyaniline Nanofibers as a Semi-Heterogeneous Catalyst in Water, *Angew. Chem., Int. Ed.*, 2007, **46**(38), 7251–7254, DOI: 10.1002/anie.200701389.
8 R. J. Tseng, J. Huang, J. Ouyang, R. B. Kaner and Yang, Polyaniline Nanofiber/Gold Nanoparticle Nonvolatile Memory, *Nano Lett.*, 2005, **5**(6), 1077–1080, DOI: 10.1021/nl050587l.
9 X. Feng, H. Huang, Q. Ye, J.-J. Zhu and W. Hou, Ag/Polypyrrole Core−Shell Nanostructures: Interface Polymerization, Characterization, and Modification by Gold Nanoparticles, *J. Phys. Chem. C*, 2007, **111**(24), 8463–8468, DOI: 10.1021/jp071140z.
10 P. Xu, X. Han, C. Wang, D. Zhou, Z. Lv, A. Wen, X. Wang and B. Zhang, Synthesis of Electromagnetic Functionalized Nickel/Polypyrrole Core/Shell Composites, *J. Phys. Chem. B*, 2008, **112**(34), 10443–10448, DOI: 10.1021/jp804327k.
11 V. Mooss, Y. Kesari and A. Athawale, Conducting Polymer and Metal-Based Sensors for the Detection of Vapours and Toxic Gases: A Concise Review, *J. Mater. NanoSci.*, 2022, **9**(1), 37–46.
12 E. K. Lai, P. D. Beattie and S. Holdcroft, Electrocatalytic Reduction of Oxygen by Platinum Microparticles Deposited on Polyaniline Films, *Synth. Met.*, 1997, **84**(1–3), 87–88.
13 F. Ficicioglu and F. Kadirgan, Electrooxidation of Ethylene Glycol on a Platinum Doped Polyaniline Electrode, *J. Electroanal. Chem.*, 1998, **451**(1–2), 95–99.
14 E. N. Zare, A. Motahari and M. Sillanpää, Nanoadsorbents Based on Conducting Polymer Nanocomposites with Main

Open Access Article. Published on 02 March 2026. Downloaded on 3/21/2026 1:02:11 PM.
This article is licensed under a Creative Commons Attribution-NonCommercial 3.0 Unported Licence.

Focus on Polyaniline and Its Derivatives for Removal of Heavy Metal Ions/Dyes: A Review, *Environ. Res.*, 2018, **162**, 173–195.

15 B. Zhang, B. Zhao, S. Huang, R. Zhang, P. Xu and H.-L. Wang, One-Pot Interfacial Synthesis of Au Nanoparticles and Au–Polyaniline Nanocomposites for Catalytic Applications, *CrystEngComm*, 2012, **14**(5), 1542–1544.

16 M. O. Ansari, M. M. Khan, S. A. Ansari and M. H. Cho, Polythiophene Nanocomposites for Photodegradation Applications: Past, Present and Future, *J. Saudi Chem. Soc.*, 2015, **19**(5), 494–504.

17 M. Jaymand, M. Hatamzadeh and Y. Omidi, Modification of Polythiophene by the Incorporation of Processable Polymeric Chains: Recent Progress in Synthesis and Applications, *Prog. Polym. Sci.*, 2015, **47**, 26–69.

18 P. E. Shaw, A. Ruseckas and I. D. W. Samuel, Exciton Diffusion Measurements in Poly(3-hexylthiophene), *Adv. Mater.*, 2008, **20**(18), 3516–3520, DOI: 10.1002/adma.200800982.

19 T. Tsumuraya, J.-H. Song and A. J. Freeman, Linear Optical Properties and Electronic Structures of Poly(3-Hexylthiophene) and Poly(3-Hexylselenophene) Crystals from First Principles, *Phys. Rev. B:Condens. Matter Mater. Phys.*, 2012, **86**(7), 075114, DOI: 10.1103/physrevb.86.075114.

20 V. C. Gonçalves and D. T. Balogh, Synthesis and Characterization of a Dye-Functionalized Polythiophene with Different Chromic Properties, *Eur. Polym. J.*, 2006, **42**(12), 3303–3310.

21 H. Bagheri, S. Banihashemi and S. Jelvani, A Polythiophene–Silver Nanocomposite for Headspace Needle Trap Extraction, *J. Chromatogr. A*, 2016, **1460**, 1–8.

22 C. Zhao, Z. Jiang, X. Cai, L. Lin, X. Lin and S. Weng, Ultrasensitive and Reliable Dopamine Sensor Based on Polythionine/AuNPs Composites, *J. Electroanal. Chem.*, 2015, **748**, 16–22.

23 R. Umeda, H. Awaji, T. Nakahodo and H. Fujihara, Nanotube Composites Consisting of Metal Nanoparticles and Polythiophene from Electropolymerization of Terthiophene-Functionalized Metal (Au, Pd) Nanoparticles, *J. Am. Chem. Soc.*, 2008, **130**(11), 3240–3241, DOI: 10.1021/ja7114212.

24 P. Pascariu, D. Vernardou, M. P. Suchea, A. Airinei, L. Ursu, S. Bucur, I. V. Tudose, O. N. Ionescu and E. Koudoumas, Tuning Electrical Properties of Polythiophene/Nickel Nanocomposites *via* Fabrication, *Mater. Des.*, 2019, **182**, 108027.

25 S.-E. Bae, K.-J. Kim, Y.-K. Hwang and S. Huh, Simple Preparation of Pd-NP/Polythiophene Nanospheres for Heterogeneous Catalysis, *J. Colloid Interface Sci.*, 2015, **456**, 93–99.

26 F. Tavares, L. V. F. Oliveira, S. Hajjar-Garreau and F. F. Camilo, Synthesis of Polythiophene-Silver Nanocomposites in Ionic Liquid for Catalytic Applications, *ACS Appl. Polym. Mater.*, 2024, **6**(7), 3756–3766, DOI: 10.1021/acsapm.3c02987.

27 C. S. Inagaki, M. M. Oliveira and A. J. G. Zarbin, Direct and One-Step Synthesis of Polythiophene/Gold Nanoparticles Thin Films through Liquid/Liquid Interfacial Polymerization, *J. Colloid Interface Sci.*, 2018, **516**, 498–510.

28 S. Chauhan, R. D'cruz, S. Faruqi, K. K. Singh, S. Varma, M. Singh and V. Karthik, Chemical Warfare Agents, *Environ. Toxicol. Pharmacol.*, 2008, **26**(2), 113–122.

29 G. S. Pearson and R. S. Magee, Critical Evaluation of Proven Chemical Weapon Destruction Technologies (IUPAC Technical Report), *Pure Appl. Chem.*, 2002, **74**(2), 187–316, DOI: 10.1351/pac200274020187.

30 B. Friedrich, D. Hoffmann, J. Renn, F. Schmaltz and M. Wolf, *One Hundred Years of Chemical Warfare: Research, Deployment, Consequences*, Springer Nature, 2017.

31 K. Kim, O. G. Tsay, D. A. Atwood and D. G. Churchill, Destruction and Detection of Chemical Warfare Agents, *Chem. Rev.*, 2011, **111**(9), 5345–5403, DOI: 10.1021/cr100193y.

32 H. Sajid, K. Ayub and T. Mahmood, Sensing Behaviour of Monocyclic C18 and B9N9 Analogues toward Chemical Warfare Agents (CWAs); Quantum Chemical Approach, *Surf. Interfaces*, 2022, **30**, 101912.

33 N. Sattar, H. Sajid, S. Tabassum, K. Ayub, T. Mahmood and M. A. Gilani, Potential Sensing of Toxic Chemical Warfare Agents (CWAs) by Twisted Nanographenes: A First Principle Approach, *Sci. Total Environ.*, 2022, **824**, 153858.

34 T. Zhang, H. Sun, F. Wang, W. Zhang, S. Tang, J. Ma, H. Gong and J. Zhang, Adsorption of Phosgene Molecule on the Transition Metal-Doped Graphene: First Principles Calculations, *Appl. Surf. Sci.*, 2017, **425**, 340–350.

35 H. Sajid, S. Khan, K. Ayub and T. Mahmood, Effective Adsorption of A-Series Chemical Warfare Agents on Graphdiyne Nanoflake: A DFT Study, *J. Mol. Model.*, 2021, **27**(4), 117.

36 U. Khanom, J. K. Saha, J. Jang and M. Rahman, Revealing Conducting Organic Polymers' Interaction with Cyanogen Halides: DFT Insights for Enhanced Gas Sensing Applications, *Struct. Chem.*, 2024, **35**(4), 1263–1272, DOI: 10.1007/s11224-023-02275-0.

37 M. S. Jyothi, V. Nagarajan and R. Chandiramouli, Investigation on Adsorption Properties of HCN and ClCN Blood Agents on Þeta–Phosphorene Nanosheets–A First–Principles Insight, *Chem. Phys.*, 2020, **538**, 110896.

38 A. McCulloch, P. Ashford and P. M. Midgley, Historic Emissions of Fluorotrichloromethane (CFC-11) Based on a Market Survey, *Atmos. Environ.*, 2001, **35**(26), 4387–4397.

39 A. R. Katritzky, O. Meth-Cohn and C. W. Rees, *Comprehensive Organic Functional Group Transformations*, Elsevier Science, 1995, pp. 211–247, ISBN 9780080447056, DOI: 10.1016/B0-08-044705-8/00257-0.

40 A. McCulloch, P. M. Midgley and P. Ashford, Releases of Refrigerant Gases (CFC-12, HCFC-22 and HFC-134a) to the Atmosphere, *Atmos. Environ.*, 2003, **37**(7), 889–902.

41 B. M. Abraham, Adsorption of Cyanogen Halides (X-CN; X= F, Cl and Br) on Pristine and Fe, Mn Doped C60: A Highly Potential Gas Sensor, *Mater. Today Commun.*, 2021, **26**, 101901.

 © 2026 The Author(s). Published by the Royal Society of Chemistry

Open Access Article. Published on 02 March 2026. Downloaded on 3/21/2026 1:02:11 PM.
This article is licensed under a Creative Commons Attribution-NonCommercial 3.0 Unported Licence.

42 S. Kim, D. C. Sorescu and J. T. Yates, Infrared Spectroscopic Study of ClCN Adsorption on Clean and Triethylenediamine-Precovered γ-Al_2O_3, *J. Phys. Chem. C*, 2007, **111**(49), 18226–18235, DOI: 10.1021/jp075409q.

43 B. Cancho, F. Ventura and M. Galceran, Simultaneous Determination of Cyanogen Chloride and Cyanogen Bromide in Treated Water at Sub-Mg/L Levels by a New Solid-Phase Microextraction–Gas Chromatographic–Electron-Capture Detection Method, *J. Chromatogr. A*, 2000, **897**(1–2), 307–315.

44 M. K. Crawford, K. D. Dobbs, R. J. Smalley, D. R. Corbin, N. Maliszewskyj, T. J. Udovic, R. R. Cavanagh, J. J. Rush and C. P. Grey, A Raman Spectroscopy Study of the Separation of Hydrofluorocarbons Using Zeolites, *J. Phys. Chem. B*, 1999, **103**(3), 431–434, DOI: 10.1021/jp9832903.

45 S. Massolo, P. Rivaro and R. Frache, Simultaneous Determination of CFC-11, CFC-12 and CFC-113 in Seawater Samples Using a Purge and Trap Gas-Chromatographic System, *Talanta*, 2009, **80**(2), 959–966.

46 E. Vessally, R. Moladoust, S. M. Mousavi-Khoshdel, M. D. Esrafili, A. Hosseinian and L. Edjlali, The ClCN Adsorption on the Pristine and Al-Doped Boron Nitride Nanosheet, Nanocage, and Nanocone: Density Functional Studies, *Thin Solid Films*, 2018, **645**, 363–369.

47 Density Functional Theory of Atoms and Molecules, in *Horizons of Quantum Chemistry*, Springer Netherlands, Dordrecht, 1980, pp. 5–15, DOI: 10.1007/978-94-009-9027-2_2.

48 S. F. Parker, J. E. Trevelyan and H. Cavaye, Vibrational Spectra of Neutral and Doped Oligothiophenes and Polythiophene, *RSC Adv.*, 2023, **13**(8), 5419–5427.

49 Y. Aoyama, T. Yamanari, N. Koumura, H. Tachikawa, M. Nagai and Y. Yoshida, Photo-Induced Oxidation of Polythiophene Derivatives: Dependence on Side Chain Structure, *Polym. Degrad. Stab.*, 2013, **98**(4), 899–903.

50 S. Chiodo, N. Russo and E. Sicilia, LANL2DZ Basis Sets Recontracted in the Framework of Density Functional Theory, *J. Chem. Phys.*, 2006, **125**(10), 104107.

51 M. J. Frisch, J. A. Pople and J. S. Binkley, Self-Consistent Molecular Orbital Methods 25. Supplementary Functions for Gaussian Basis Sets, *J. Chem. Phys.*, 1984, **80**(7), 3265–3269.

52 F. Lipparini, F. Egidi, J. Goings, B. Peng, A. Petrone, T. Henderson, D. Ranasinghe, V. G. Zakrzewski, J. Gao and N. Rega, *Gaussian 16*, Wallingford, CT, 2016.

53 S. Grimme, Accurate Description of van Der Waals Complexes by Density Functional Theory Including Empirical Corrections, *J. Comput. Chem.*, 2004, **25**(12), 1463–1473, DOI: 10.1002/jcc.20078.

54 S. Grimme, Semiempirical GGA-type Density Functional Constructed with a Long-range Dispersion Correction, *J. Comput. Chem.*, 2006, **27**(15), 1787–1799, DOI: 10.1002/jcc.20495.

55 *Zhao: Benchmark databases for nonbonded interactions… – Google Scholar*. https://scholar.google.com/scholar_lookup?title=Benchmark%20databases%20for%20nonbonded%20interactions%20and%20their%20use%20to%20test%20density%20functional%20theory&publication_year=2005&author=Y.%20Zhao&author=D.G.%20Truhlar accessed 2022-09-06.

56 M. Asif, H. Sajid, K. Ayub, M. Ans and T. Mahmood, A First Principles Study on Electrochemical Sensing of Highly Toxic Pesticides by Using Porous C4N Nanoflake, *J. Phys. Chem. Solids*, 2022, **160**, 110345.

57 T. Lu and F. Chen, Multiwfn: A Multifunctional Wavefunction Analyzer, *J. Comput. Chem.*, 2012, **33**(5), 580–592.

58 W. Humphrey, A. Dalke and K. Schulten, VMD: Visual Molecular Dynamics, *J. Mol. Graphics*, 1996, **14**(1), 33–38.

59 H. Ullah, A.-H. A. Shah, K. Ayub and S. Bilal, Density Functional Theory Study of Poly(*o*-Phenylenediamine) Oligomers, *J. Phys. Chem. C*, 2013, **117**(8), 4069–4078, DOI: 10.1021/jp311526u.

60 H. Ullah, A.-H. A. Shah, S. Bilal and K. Ayub, DFT Study of Polyaniline NH_3, CO_2, and CO Gas Sensors: Comparison with Recent Experimental Data, *J. Phys. Chem. C*, 2013, **117**(45), 23701–23711, DOI: 10.1021/jp407132c.

61 R. P. McCall, J. M. Ginder, J. M. Leng, H. J. Ye, S. K. Manohar, J. G. Masters, G. E. Asturias, A. G. MacDiarmid and A. J. Epstein, Spectroscopy and Defect States in Polyaniline, *Phys. Rev. B:Condens. Matter Mater. Phys.*, 1990, **41**(8), 5202–5213, DOI: 10.1103/physrevb.41.5202.

62 U. Salzner, J. B. Lagowski, P. G. Pickup and R. A. Poirier, Comparison of Geometries and Electronic Structures of Polyacetylene, Polyborole, Polycyclopentadiene, Polypyrrole, Polyfuran, Polysilole, Polyphosphole, Polythiophene, Polyselenophene and Polytellurophene, *Synth. Met.*, 1998, **96**(3), 177–189.

63 X.-Y. Liang, N. Ding, S.-P. Ng and C.-M. L. Wu, Adsorption of Gas Molecules on Ga-Doped Graphene and Effect of Applied Electric Field: A DFT Study, *Appl. Surf. Sci.*, 2017, **411**, 11–17.

64 S. Garg, R. Singla and N. Goel, DFT Study on the Spin States of Polyaniline–3d Transition-Metal (Sc–Zn) Composites and Their Sensing Application to Detect Chemical Warfare Agents, *J. Phys. Chem. A*, 2024, **128**(4), 773–784, DOI: 10.1021/acs.jpca.3c07114.

65 M. Sun, Q. Ren, Y. Zhao, J.-P. Chou, J. Yu and W. Tang, Electronic and Magnetic Properties of 4d Series Transition Metal Substituted Graphene: A First-Principles Study, *Carbon*, 2017, **120**, 265–273.

66 X.-Y. Liu, H. Zhang and X.-L. Cheng, Tuning the Electronic and Magnetic Properties of In-Planar Graphene/Boron Nitride Heterostructure by Doping 3d Transition Metal Atom, *J. Phys. Chem. C*, 2019, **123**(36), 22403–22412, DOI: 10.1021/acs.jpcc.9b06537.

67 P. Kolandaivel and V. Nirmala, Study of Proper and Improper Hydrogen Bonding Using Bader's Atoms in Molecules (AIM) Theory and NBO Analysis, *J. Mol. Struct.*, 2004, **694**(1), 33–38, DOI: 10.1016/j.molstruc.2004.01.030.